

Controlling Mixing at the Interaction Zone Through Systematic Variation of the Inlet Rotor Cavity Volume and Length Scale.

Konstantinos G. Barmपालias¹, Anestis I. Kalfas², Reza S. Abhari¹, Toshio Hirano³, Naoki Shibukawa³ and Sasaki Takashi³

¹Laboratory for Energy Conversion
Department of Mechanical and Process Engineering, ETH Zurich
Sonneggstr. 3 ML J33, CH-8092, Zurich, Switzerland

²Aristotle University of Thessaloniki, Thessaloniki, Greece

³Toshiba Corporation, Yokohama, Japan

ABSTRACT

Mixing losses due to cavity related flows in axial steam turbines contribute considerably to overall aerodynamic losses. The coherent study presented in this paper examines the influence of rotor inlet cavity geometry on stage efficiency. The experimental work is supported by computational analysis. Inlet cavity geometry has been varied by reducing the axial and radial cavity lengths along with the volume. Six different configurations have been examined, focusing mainly on the flow interactions occurring at the zone between the cavity and main flow and their impact on stage efficiency. An upper stator-casing platform prolonged by 17% and 34%, and a radial wall length shortened by 13% and 25% offered a cavity volume reduction of 14% and 28%, respectively, compared to the initial cavity volume. The axial cavity wall length reduction impacts drastically on the vortex formation inside the cavity. A 17% length reduction leads initially to the bifurcation and re-connection of the vortex during inflow, whereas the 34% length reduction completely eliminates the presence of any vortex. On the other hand, the radial cavity wall length reduction affects the vortex positioning. Generally, the cases with radial wall length reduction show higher efficiency relative to the axial cavity length reduction. For the 14% cavity volume reduction cases this difference rises to 1%, and for the 28% cavity volume reduction the difference is even higher, attaining a 1.7% efficiency increase.

NOMENCLATURE

a	cavity axial wall length
b	cavity radial wall length
c	normalized cavity axial length
C_{pt}	pressure coefficient $(P_t - P_{s,exit}) / (P_{t,inlet} - P_{s,exit})$
F	force
h	normalized blade span
P	pressure
r	radius
r_z	radius of the streamline
R1	1 st rotor
R2	2 nd rotor
S1	1 st stator
S2	2 nd stator
v	velocity
V	volume

Greek

α	absolute flow yaw angle
γ	flow pitch angle
ρ	density

Abbreviations

CV	cavity volume
ConV	control volume
CVR	cavity volume reduction
HS	high solidity
LS	low solidity
Δeff	efficiency difference

Subscript

r	radial direction
s	static
t	total
z	axial direction
θ	tangential direction

INTRODUCTION

Modern turbomachinery design aims to increase blade loading and the pressure ratio while maintaining and even increasing efficiency. With this perspective, secondary flows, unsteady blade-to-blade and vortex-to-blade interactions and the interactions between the leakage and main flows contribute considerably to the overall turbine losses. Aerodynamic losses owing to secondary flow effects have long been under investigation. Particularly in low-aspect ratio blading the secondary flow effects are dominant in the overall loss mechanism, [1, 2, 3]. Denton [4] attributes a large part of these losses, almost 1/3 of the total aerodynamic losses in axial turbines, to the mixing occurring at the interaction zone. The leakage flow that re-enters the main stream has a different momentum and flow angle and mixes out with the main flow. Gier et al. [5] performed a loss breakdown for inner and outer cavities and concluded that 60% of the losses caused by the cavities are due to the mixing during leakage flow re-entry. Therefore, controlling the path of the exiting leakage flow is crucial. With the use of bladelets, either in the stationary system [6], or on the rotor shroud itself [7], the control of shroud leakage has been attempted. Schlienger et al. [8] attempted to improve the re-entry of the leakage flow with the use of inserts. Curtis et al. [9], used an air-curtain to reduce the shroud leakage. A jet angled at 45 degrees to the axial direction provided opposing momentum to the shroud leakage flow and an efficiency gain of 0.4% was measured. Apart from the mixing itself occurring at the

interaction zone, the egress of the leakage flow impacts on the subsequent stator. Anker et al. [10] carried out work on the strengthening of the upper passage vortex. Pau et al. [11] showed the enhancement of all counter-rotating vortices with respect to the main passage vortex due to the low turning experienced by the leakage flow. The strong negatively signed vorticity dominating the secondary flows at the interaction zone has also been reported by Adami et al. [12]. Li et al. [13] reported on the influence of leakage flows even after 2 bladerows. Hunter and Manwaring [14] on the same topic and using ethylene tracer gas, traced the low momentum fluid at the downstream rotor row and two additional vortices in the following stator passage associated with the radial variation in the circumferential flow angle of the upstream rotor. Flow visualization has also been carried out by Vakili et al. [15]. Through their PIV measurements they reported on the significance for leakage reduction of the fin axial location and angle and the step height. Flow visualization was also used by Rhode et al. [16], [17] to measure the leakage resistance with respect to step shape and height. Pfau et al. [18], [19], carried out a detailed study of the dominant kinematic flow feature in the cavity region, the toroidal vortex residing in the cavity and derived design recommendations to make use of the interaction flow.

Most of the studies on cavity flows deal with the interaction between the two flows at the rotor exit cavity, the mixing that occurs and their impact on the downstream bladerows. This work focuses however on the interaction zone of the rotor inlet cavity and the associated interaction between the leakage and main flows at the rotor inlet. The different geometries of the rotor inlet cavity created by cavity volume and length scale modifications affect the leakage re-entry path. Geometry changes create changes in the toroidal vortex that handles the in and out flows. The exact place and timing of the fluid egress impacts on the efficiency through the leakage flow that exits the cavity facilitating the tip passage vortex.

INLET CAVITY CONFIGURATIONS

The research turbine has a sealing configuration of 4 seals with a gap of 0.44% of the blade span. The inlet cavity under investigation is the one illustrated in Figure 1 and corresponds to the baseline case. The dimensions are $0.24C_z$ and $0.36C_z$, respectively, in the axial and radial directions, which provide a minimum safety operating distance of $0.16C_z$ between the rotor shroud and stator casing (Figure 1). The test cases examined in this study are shown in Figure 3. The cavity sizes under investigation are 14% and 28% smaller than the baseline case. The volume reduction is accomplished either by an extension of the upper stator casing platform or by a reduction of the cavity's radial wall. The six cases are divided into two groups. In every group the cavity volume is kept constant so as to exclude any influence of the cavity volume on the mass flow that escapes through the labyrinth over the rotor. In the two cases where the upper stator casing platform was extended, the cavity's axial length was reduced by 17% and 34% respectively, as shown in Figures 3a and 3d. The radial wall length was reduced by 14% and 25%, (Figures 3b, 3c, 3e and 3f) to achieve the cavity volume reductions of 14% and 28% respectively. The lowering of the upper axial cavity wall was intended to create a more circular cavity vortex by eliminating the area where fluid was originally drifting between the cavity vortex and the wall. The design intention of the additional curvature of the cases presented in Figure 3c and 3f was to eliminate the counter-rotating vortex that resides in the corner formed between the downstream radial cavity wall and the upper axial wall. All cases originated from the baseline case with the use of extensions. The extensions are depicted in red in Figure 3.

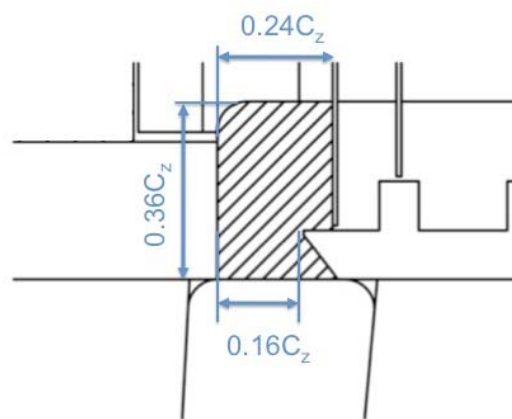


Fig. 1 Illustration of the inlet cavity

EXPERIMENTAL METHOD

The research facility

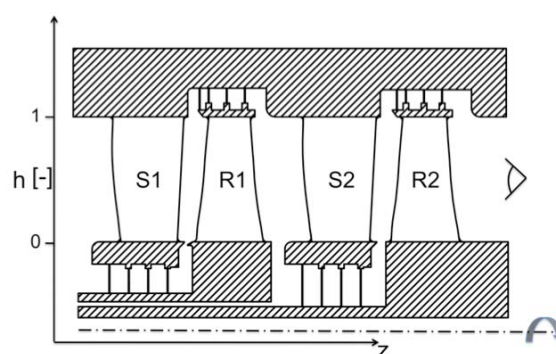


Fig. 2 Schematic diagram of the two-stage axial turbine

The measurements were performed in the 'LISA' two-stage axial research turbine at the Laboratory for Energy Conversion (LEC) of ETH Zurich (Figure 2). The turbine inlet temperature TET is kept constant at 310 K, with an accuracy of 0.9 K. A DC generator maintains a constant operating speed of 2750 ± 0.5 RPM ($\pm 0.02\%$). The measurement uncertainty of the test facility concerning total-to-static efficiency of the second stage is $\pm 0.21\%$. A more detailed description of the test facility is available in Schlienger et al. [20]. The stator blade row configurations differ as shown in Table 1. The first stator is of a high solidity ($\sigma = 1.43$) design, whereas the second stator has a low solidity ($\sigma = 1.25$). Both stators are designed to have the same exit flow angle and axial chord. The associated operating parameters based on the LS stator are summarized in Table 2. More detailed measurements on the baseline test case can be found in Tashima et al. [21].

Table. 1 Geometric details of stator blades.
(* Indicates that the dimension is measured at 50% span)

Parameter	HS stator	LS stator
Blade count Z_s	48	36
Axial chord* C_z [mm]	50	50
Chord length* C [mm]	66.3	77.4
Pitch* T [mm]	46.5	62.0
Blade span H [mm]	90	90
Aspect ratio $AR = H/C$ [-]	1.36	1.16
Solidity $\sigma = C/T$ [-]	1.43	1.25

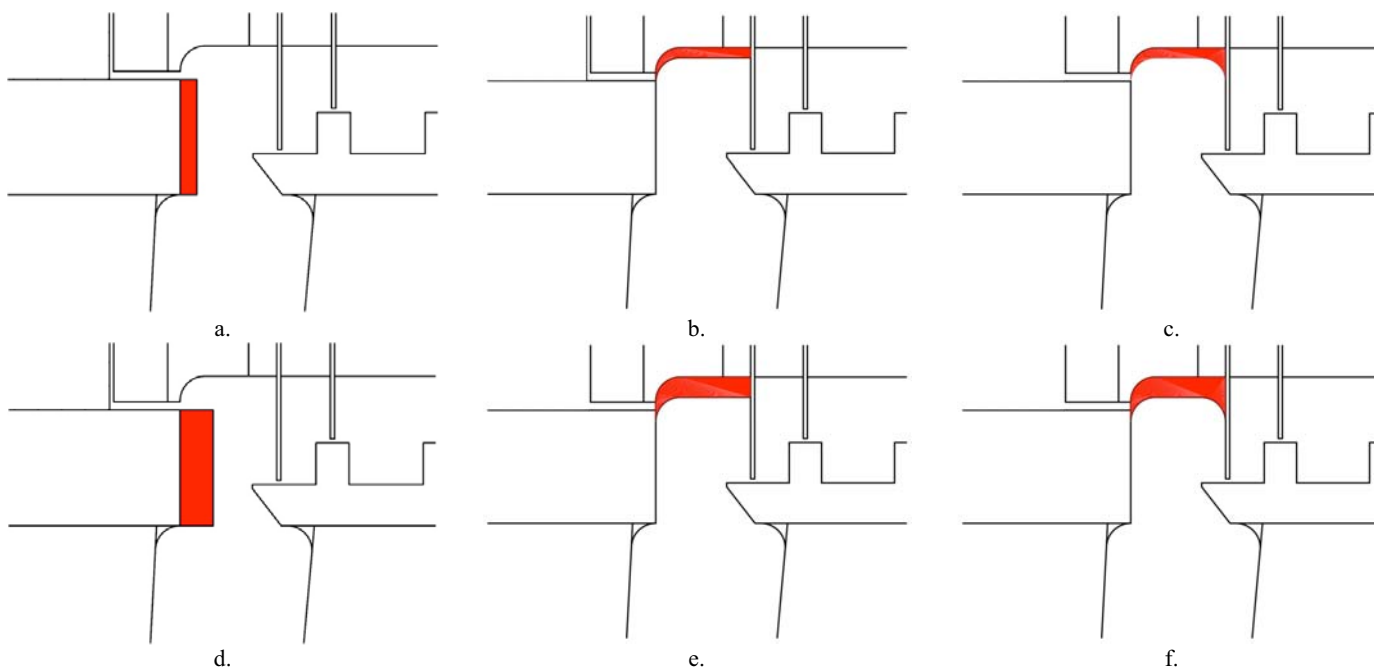


Fig. 3 Inlet cavity configurations. Cavity volume reduction 14% for (a), (b) and (c), and cavity volume reduction of 28% for (d), (e) and (f). Extension of the upper casing stator platform by a. 17% and d. 34% of the cavity’s axial length and shortening of the radial wall length by 13% for (b) and (c), and 25% for (e) and (f).

Instrumentation

Both steady and unsteady flow field measurements are made. In the main flow the steady flow field is measured using a 5-hole pneumatic probe (5HP) with a 0.9 mm head diameter, whereas the unsteady flow field is captured with the use of a 2-sensor Fast Response Aerodynamic Probe (FRAP), which has a 1.8 mm head diameter as shown in Figure 4. For the measurements inside the cavity, a miniature 4-hole pneumatic probe (4HP) was used for the steady flow field, together with a pair of miniature FRAP probes of 0.84mm head diameter for the unsteady flow field. Each miniature FRAP probe is one-holed; one miniature FRAP is yaw sensitive and the other is used for the pitch measurement. A detailed description of the two miniature probes can be found in Pfau et al. [22] The FRAP has a measurement bandwidth of 48 kHz. The measured flow parameters and their absolute uncertainties are listed in Table 3. Absolute uncertainties of the measured flow quantities in Table 3 are expressed as a percentage of the calibration range for the angles, a percentage of the dynamic head for pressures and a percentage of the absolute Mach number for the velocity. The use of FRAP and pneumatic probes in the ‘LISA’ turbine facility has been detailed in several publications, including Lenherr et al. [23].

Table. 2 Main parameters of the test case configuration based on the characteristics of the LS stator.

Rotor speed [RPM]	2750
Overall pressure ratio [-]	1.32
Mass flow [kg/sec]	7.87
Turbine inlet temperature [°C]	37.8
Blade number count stage-1 (stator/rotor)	48/48
Blade number count stage-2 (stator/rotor)	36/48
Tip/hub diameter [mm]	800/620
Flow coefficient (stage-2) [-]	0.3
Loading coefficient (stage-2) [-]	1.0
Mach number (stator/rotor)	0.32/0.1
Reynolds number (rotor)	2×10^5

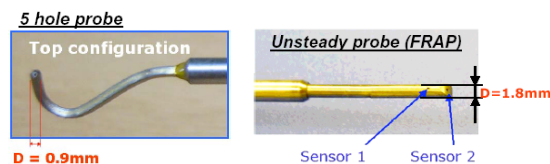


Fig. 4 5HP and 2-sensor FRAP measurement probes

Table. 3 Absolute uncertainties in probe measurements for a calibration range of yaw $\pm 30^\circ$ pitch $\pm 20^\circ$ and for a Mach number of 0.3. (uncertainties in pressure are shown as a percentage of dynamic head, uncertainties in Mach number are shown as a percentage of the absolute Mach number).

	α	γ	P_t	P_s	M
FRAP	0.5°	0.7°	1%	1.2%	1%
5HP	0.3°	0.3°	1.8%	2%	0.06%

Probe measurements were made at the rotor exit and downstream of the LS stator. Measurements at the stator exit were made 6mm downstream of the stator at $h=1$ while inside the cavity. The measurement plane is located at $0.224C_z$ downstream of the 2nd stator’s trailing edge at midspan. The measurement grids consist of 48 points and 61 points evenly distributed in the radial and circumferential directions. The circumferential traverse was conducted over three LS stator pitches. Data are sampled at 200 kHz, which corresponds to 92 samples per blade passing period. A phase-lock data-averaging procedure was subsequently performed over 90 revolutions.

Numerical method

The numerical study presented in this paper was performed using the ANSYS CFX flow solver. The second stage of the turbine (Figure 5a) was meshed using an unstructured mesh with 8 million nodes, as shown in Figure 5b. The stator-rotor blade count ratio of the second stage is 3:4. As the periodicity is related to the stator-rotor blade count ratio, 30 degrees were meshed, i.e. three

stator passages and four rotor passages. The y^+ values on the walls were all below 30. The flow solver was run in unsteady mode using the transient rotor-stator interface. The results of the steady simulations were used as initial conditions. A reduction of the maximum mean square value for the residual from 10^{-2} to 10^{-6} was used as a convergence criterion. The standard k- ϵ turbulence model with a turbulence intensity of 5% at the inflow boundary layer was employed. The experimentally measured mass-averaged total pressure, together with the flow angle distribution and the static temperature constituted the boundary conditions at the inflow, whereas at the outflow the measured static pressure distribution was used for the steady simulation, which provided a good initial solution. The circumferential boundaries are periodic and a no-slip condition was applied at the adiabatic walls.

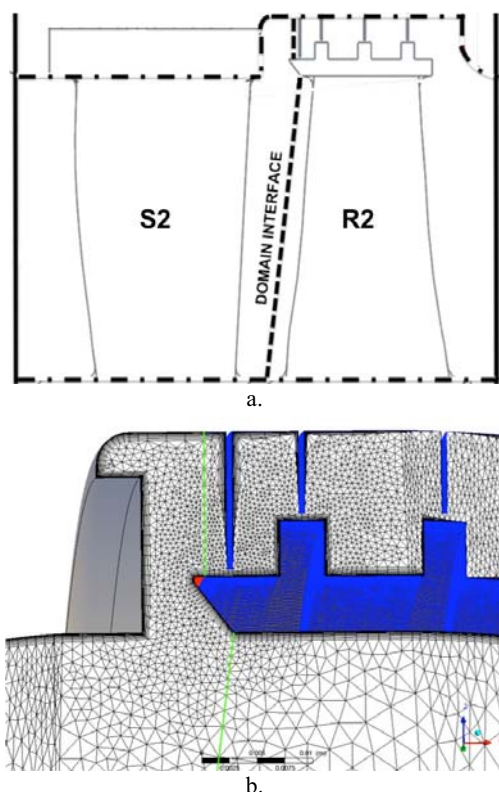


Fig. 5 The simulation domain is bordered by the measurement planes, solid lines at stage inlet and outlet. The center line sketches the simplified fluid path without the stator hub cavity. The domain interface is indicated by the dashed line.

Validation

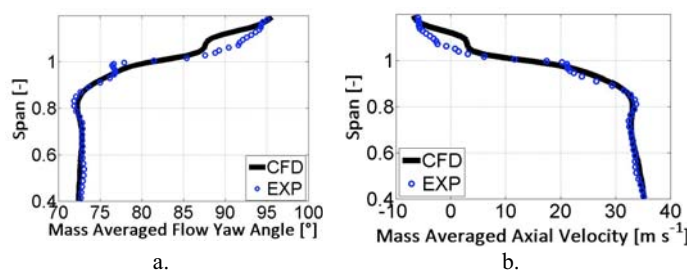


Fig. 6 Comparison of experiment and CFD for (a) the pitchwise mass-averaged flow yaw angle distribution and (b) the pitchwise mass-averaged axial velocity distribution at stator exit.

Figure 6 shows the comparison of experimental and numerical data of the pitchwise mass-averaged flow yaw angle and axial

velocity distribution at the stator exit. There is a very good agreement within 0.5 degrees for the yaw angle up to 0.95 of the span. The CFD does not predict the underturning of the flow close to the upper casing. Moreover, inside the cavity because of the strong secondary flows, the difference between experimental and computed results rises by up to 5 degrees. The pitchwise mass-averaged axial velocity shows a very good agreement over the blade span. The difference is within 1 m/s. Inside the cavity, although the trend is captured, the CFD predicts higher velocities.

RESULTS AND DISCUSSION

The experimentally measured stage efficiency for the cases considered in this study is shown in Figure 7. Overall the radial wall length reduction performs better than the axial reduction for both the 14% CVR and 28% CVR cases. For cases 14.2 and 28.2, the use of the additional curvature between the upper axial cavity wall and the downstream radial wall does not act beneficially. It offers a 0.15% efficiency gain for case 14.2 compared to case 14.1 and an efficiency fall of 0.7% for case 28.2 compared to case 28.1.

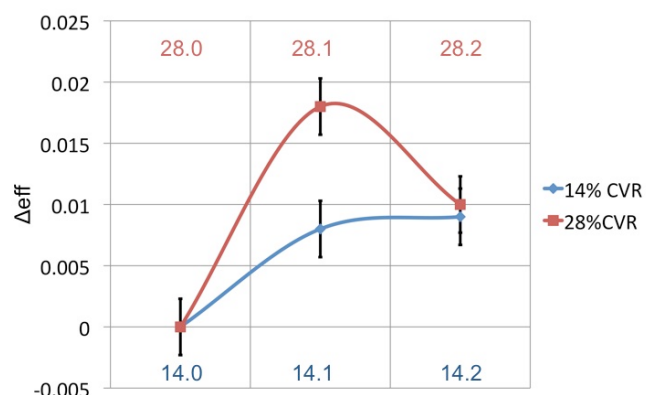


Fig. 7 Δeff for the cases examined in this study. Cases 14.0 and 28.0 are used as references for the cases with the same CVR

The experimentally measured pitchwise mass-averaged total pressure loss coefficient is shown in Figure 8a for the cases with 14% cavity volume reduction and in Figure 8b for the cases with 28% cavity volume reduction. No measurable differences are identified in the main flow for the cases with 14% CVR. The stator casing platform extension of the 14.0 case does not influence the formation of the boundary layer on the casing. The axial cavity wall length reduction leads to lower pressure inside the cavity, which potentially decreases the leakage mass flow through the labyrinth. The comparison between the cases with 28% CVR shows an area of lower loss being generated at the tip section of the blade in the region of the casing’s boundary layer. The extension of the stator casing platform acts beneficially.

The experimentally measured pitchwise mass-averaged relative flow yaw angle is shown in Figure 9a for the cases with 14% cavity volume reduction and in Figure 9b for the cases with 28% cavity volume reduction. For the cases with 14% CVR the 14.1 case exhibits a smaller tip passage vortex when compared to cases 14.0 and 14.2. The straight black line from 0.6 to 0.85 of the span coincides with the designed metal exit angle of the rotor blade. For the 28% CVR cases, cases 28.0 and 28.2 resemble each other, with case 28.1 being different. The tip passage vortex in case 28.1 is located at a lower span position compared to cases 28.0 and 28.2. This also causes some disturbance in the flow underneath at 0.4 span.

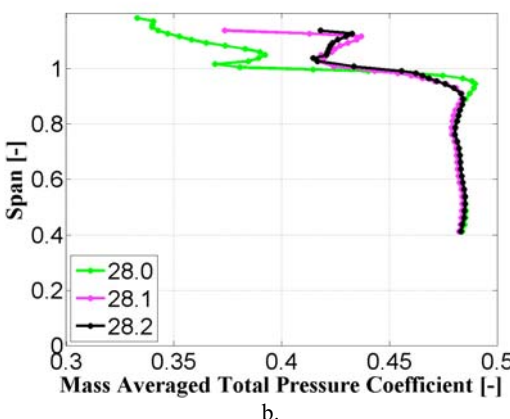
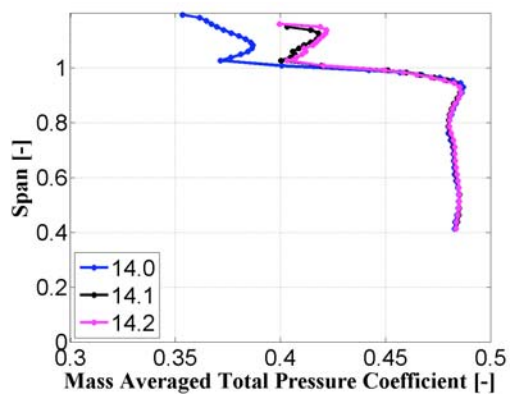


Fig. 8 Experimentally measured pitchwise mass-averaged total pressure coefficient for the cases with 14% CVR (a) and the cases with 28% CVR (b). Stator exit

In Figure 10, the computed radial velocity distribution is plotted on a meridional plane at the exit of the stator and for $h=0.95$ till $h=1.18$, for all cases examined in this study. The red colour indicates upward fluid movement. The plot is for a time instant and during inflow to the cavity. The 14% CVR cases are presented in Figures 10a, 10b and 10c and the 28% CVR cases in Figures 10d, 10e and 10f. Secondary flow vectors are projected onto the plane. White lines denote the flow path.

Great differences are present between the cases of axial and radial CVR for the same volume. The ratio of axial to radial wall length, presented in Table 4, has a direct impact on the vortex formation inside the cavity. The vortex formed in the 14.0 case has an ellipsoidal shape owing to the ratio of the cavity wall length. The rectangular cavity shape with a ratio of axial to radial wall length of 0.55 stretches the vortex in the radial direction. To the contrary, the radial wall length reduction of cases 14.1 and 14.2 leads to the formation of a more circular vortex with its centre located at a lower radial position compared to case 14.0. The radial wall length reduction offers an efficiency improvement. The upper 15% of the cavity was dominated by the counter-rotating vortex and fluid residing between the main cavity vortex and the wall. The lowering of the upper axial wall by 14% in case 14.1 eliminated the fluid that previously drifted between the cavity vortex and the upper axial wall leading to extra losses.

Table. 4 Ratios of cavity’s axial to radial wall length

Case	14.0	14.1/14.2	28.0	28.1/28.2
a/b	0.55	0.77	0.44	0.9

Even greater differences in efficiency are measured for the 28% CVR group between the cases examined. The difference in the ratio of the axial to radial cavity wall is apparent when comparing case 28.0, which has $a/b=0.44$, with case 28.1 that has an $a/b=0.9$. The almost square cavity shape provided an efficiency increase of 1.8% relative to the rectangular shape of case 28.0. As has been presented in detail and discussed by Barmpalias et al. [24], the ratio of $a/b=0.44$ eliminates the presence of the cavity vortex that continuously and smoothly regulated the in and outflows and strong radial jets dominated the cavity flow. These jets penetrate the main flow, abruptly redirect the flow from an axial to a radial direction and cause extensive mixing at the interaction zone. To the contrary, the almost square cavity of case 28.1 provides a great efficiency advantage. The drifting mass flow between the cavity vortex and the wall is also not present. The vortex core has now migrated to a lower span position, though still extending within the cavity area. The lower end of the cavity vortex during outflow reaches the interaction zone. The fluid that exits the inlet cavity is already oriented in the axial direction and a smooth re-entry angle is achieved. On the other hand, the rectangular cavity shape demands a radial transport of the fluid inside the cavity, since the cavity vortex is stretched and at a higher span location. In such a case the fluid will intersect with the main flow and will be abruptly re-directed to the axial direction, thus being a major source of loss generation.

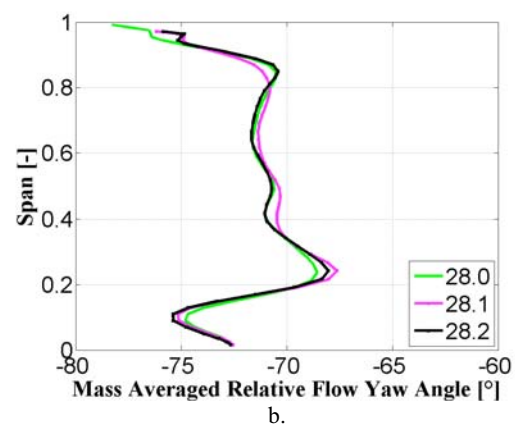
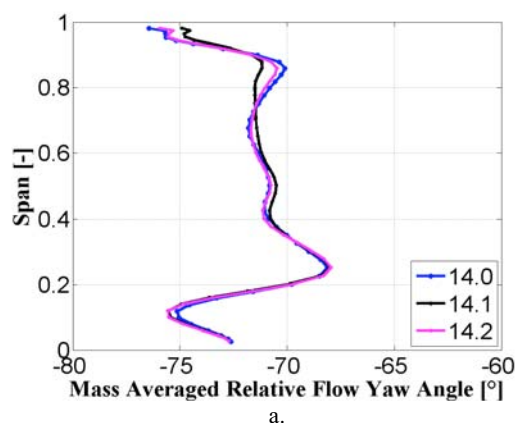


Fig. 9 Experimentally measured pitchwise mass-averaged relative flow yaw angle for the cases with 14% CVR (a) and the cases with 28% CVR (b). Rotor exit

The flow path inside the cavity plays a key role inside the cavity. Nevertheless, the path of the mass flow that is to enter the cavity is of great importance. The flow that exits the stator blade passage and is within the upper 10% of the blade span is quick to enter the cavity or interact with the cavity flows. Figure 11 shows a

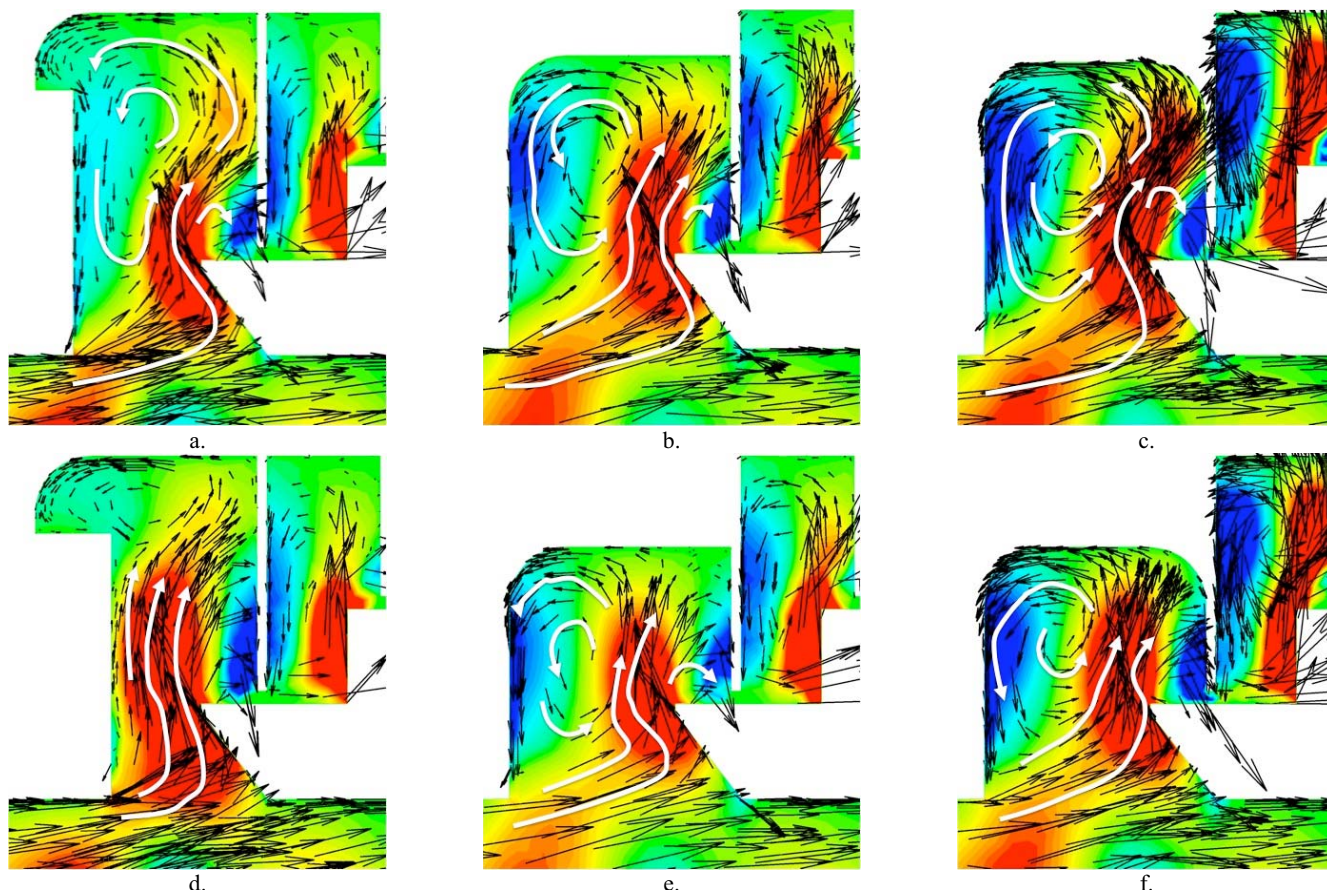


Fig. 10 CFD computed results of the inflow for cases (a) 14.0, (b) 14.1, (c) 14.2, (d) 28.0, (e) 28.1, and (f) 28.2. The simulations show a meridional cut. The planes are colored with radial velocity and the secondary flow vectors are projected onto them. The flow paths are denoted by white lines.

streamline that exits the stator and enters the cavity. The control volume presented in Figure 11 is bordered by the axial planes located at $c=0$ and $c=1$. For cases 14.0 and 28.0, the upstream axial plane is taken at $c=0.17$ and $c=0.34$, respectively. The inner surface was chosen to be at $h=0.9$. At this radial location the area integration delivers a net radial mass flow of approximately 0. The outer surface is at $h=1.0$, the interaction zone between the cavity and main flows. The local pressure gradient across this control volume is not sufficient to keep the flow at a constant radius. Streamlines originating from the stator side enter the cavity. There are three driving mechanisms that bend the streamline upwards and inside the cavity: The radial pressure gradient between the two radial locations, the sudden area increase due to the cavity and the sucking of the leakage mass flow. For the case under study, the radial equilibrium can be simplified to

$$\frac{v_z^2}{r_z} - \frac{v_\theta^2}{r} = -\frac{1}{\rho} \frac{\partial p}{\partial r} + \frac{F_r}{\rho V_{ConV}} \quad (1)$$

assuming that the mean streamline enters the control volume axially. Using CFD computed values over the control volume a representative streamline with an average meridian radius of $r_c=13\text{mm}$ is calculated for all cases examined. For the cases with radial wall length shortening, the streamline enters the cavity at $c=0.8$. This coincides with the CFD results in Figure 10, where most of the inflow to the cavity takes place from $c=0.8$ to $c=1.0$. For the cases with axial wall length reduction, as the streamline

curvature remains unaltered the main inflow region is moved to a more downstream position. The same streamline now impinges on the inclined surface of the shroud and is abruptly redirected

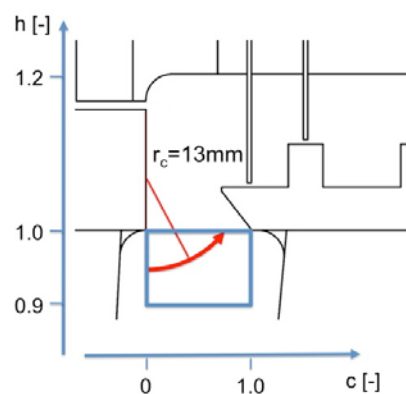


Fig. 11 Streamline curvature of the mean streamline that enters the control volume bordered axially by planes at cavity inlet and exit and radially at $h=1$ and $h=0.9$.

from the axial direction radially upwards, forming a strong jet. Even though the overall mass flow leaking through the labyrinth remains the same for all cases examined, the stronger jet formed in cases 14.0 and 28.0 leads to greater mixing at the interaction zone, therefore generating more losses.

In Figure 12, the radial sum mass flux at the cavity inlet from $c=0.85$ to $c=1.0$ is plotted where most of the inflow takes place.

The mass flux is axially summed over the last 15% of the cavity inlet. As seen in Figure 12, the peak values for case 14.0 are increased up to 60% and 66% compared to the 14.1 and 14.2 cases, respectively. The formation of a strong jet in case 14.0 in the last 15% of the cavity inlet leads to increased mixing through abrupt fluid flow re-direction, causing efficiency deficits compared to the 14.1 and 14.2 cases. In Figure 12b, the radial sum mass flux in the last 15% of the cavity inlet is presented for the cases with 28% cavity volume reduction. Case 28.0 shows an

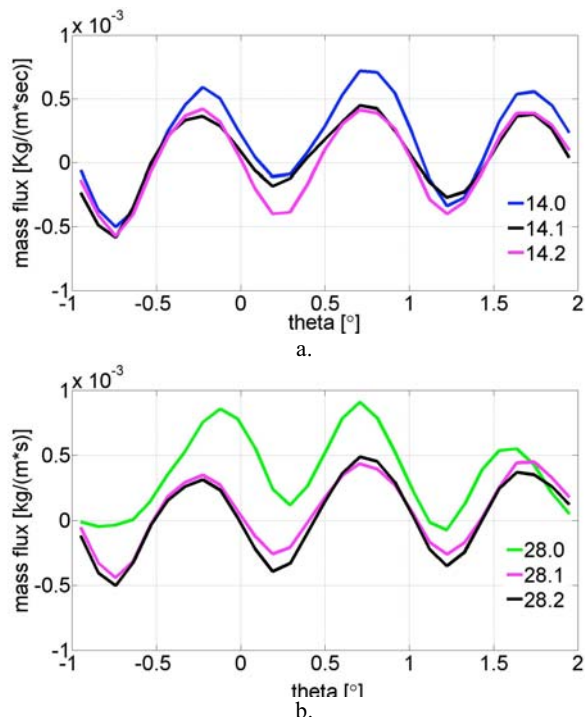


Fig. 12 Computed (steady CFD) mass flux at cavity inlet from $c=0.85$ till $c=1$ for the cases with (a) 14% CVR and (b) 28% CVR. Data are axially summed

increase in peak values of 100% compared to the 28.1 and 28.2 cases. This leads to a considerable increase in the mixing and in the flow disturbance and impacts negatively on efficiency for the 28.0 case.

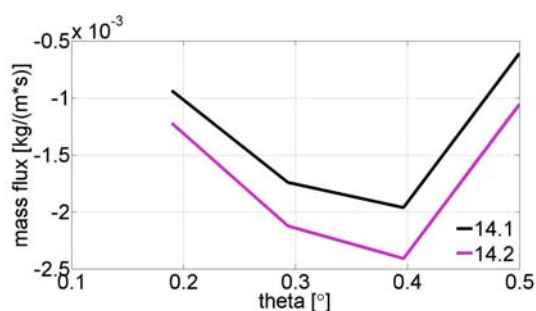


Fig. 13 Computed (steady CFD) mass flux for cases 14.1 and 14.2 summed from $c=0$ to $c=0.17$ at the circumferential location where the outflow from the cavity takes place.

The curvature introduced between the upper axial wall and the downstream radial wall in cases 14.2 and 28.2 intensifies the vortex of the cavity. Although designed to eliminate the counter-rotating vortex of the upper right corner of the cavity and to assist the flow re-direction from a radial to an axial direction, the curvature does not act beneficially. The mass flow initially trapped in the counter-rotating vortex is now circulating into the main vortex of the cavity. Therefore, more mass flow is

exchanged in the interaction zone between the cavity and main flows and more mixing takes place. In Figure 13, the mass flux from $c=0$ to $c=0.17$ axially averaged, is plotted for cases 14.1 and 14.2 during the outflow from the cavity. The peak values of the outflow for case 14.2 are increased by 25% compared to case 14.1. This is owing to the mass flow that is re-directed axially upstream and then radially downwards because of the rounding of the upper right corner of the cavity. The situation is identical in cases 28.1 and 28.2.

As already shown, the curvature introduced at the upper right cavity corner increases the mass flow that is re-directed towards the main cavity vortex. The flow that enters the cavity once it reaches the upper axial wall will be re-directed left or right (Figure 14a). A percentage of the mass flow that initially enters the cavity is redirected left to the main cavity vortex. This mass flow will later interact with the main flow at the interaction zone. The remaining mass flow turns right to feed the counter-rotating vortex. Part of the mass flow of the counter-rotating vortex will escape through the cavity over the rotor. The left and right vortices are shown in Figure 14a. The graph in Figure 14b presents the percentage of the flow that follows the left or the right vortex. The data were taken from a $z-\theta$ plane at $h=1.07$, as shown in Figure 14a. The rounding of the upper corner of the 14.2 and 28.2 cases redirects 13% and 8% more flow to the left vortex compared to cases 14.1 and 28.1 respectively. The high percentage of the right vortex for case 28.0 is due to the fact that the toroidal cavity vortex has given its place to strong radially moving jets that wash in and out of the cavity, as shown by Barmpalias et al. [24]

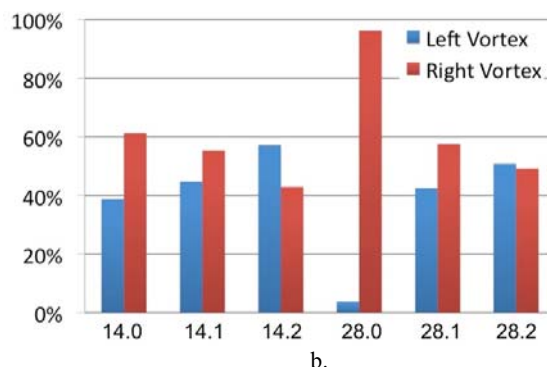
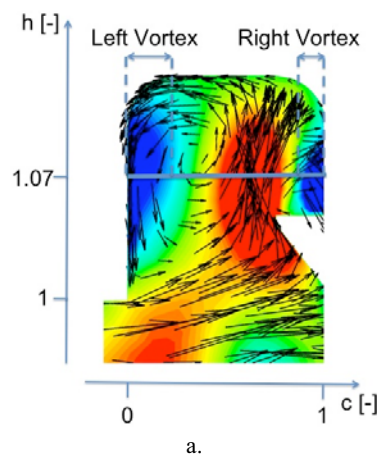


Fig. 14 Distribution of the flow between the left and the right vortex on a $z-\theta$ plane at the radial height of $h=1.07$.

CONCLUSIONS

This paper examines the impact of the mixing process occurring at the interaction zone between the cavity and main flows. A series of experiments has been carried out to investigate

the influence on efficiency of six different rotor inlet cavity designs that modify the cavity volume along with the length. Experimental results were supported by computational analysis. The initial cavity volume of the baseline case was reduced by 14% and 28%. This was achieved by extending either the upper casing stator platform or through a radial wall length reduction.

In both the 14% and 28% groups the cases with radial wall length reduction performed better. The radial wall length reduction in the 14% case had an efficiency gain of 0.85%. Following the same trend, the radial wall length reduction of 28%, (case 28.1) showed an efficiency benefit of 1.7% compared to case 28.0, the baseline case. This is due to the presence of the strong radial jets that replaced the cavity vortex, causing extra losses in case 28.0.

The additional curvature introduced in the upper right corner of the cavity increased the efficiency by 0.15% in the 14% CVR group, which is within the efficiency accuracy measurement of the test facility. In the case of the 28% CVR group the efficiency decreased by 0.7% owing to the increased mass flow that was circulated by the cavity vortex and interacted with the main flow. The additional mass flow originated from the mass flow that was trapped in the counter-rotating vortex of the upper right corner.

This study suggests that the square shaped cavity performs better than the rectangular cavity. Additionally, the presence of corners inside the cavity is beneficial, as the mass flow trapped does not interact with the main flow. Nevertheless, the turbine designer has to account for all reasons responsible for creating losses and balance them against each other.

ACKNOWLEDGEMENTS

The authors acknowledge the significant contributions of Mr. Tsuguhisa Tashima, Prof. Tadashi Tanuma and Dr. Hideo Nomoto of Toshiba in the design and development of the inlet cavity configurations. We also thank the Toshiba Corporation for their kind permission to publish part of these data.

REFERENCES

- [1] Langston, L. S., 2001, "Secondary Flows In Axial Turbines – A Review," *Annals of the New York Academy of Sciences*, Vol. 934(1), pp. 11-26
- [2] Chaluvadi, V. S. P., Kalfas, A. I. and Hodson, H. P., 2001, "Blade Row Interaction In a High-Pressure Steam Turbine," *Journal of Turbomachinery*, Vol. 125, pp. 14-24
- [3] Hodson, H. P. and Howell, R. J., 2005, "Bladerow Interactions, Transition and High-Lift Aerofoils in Low-Pressure Turbines," *Annual Reviews of Fluid Mechanics*, Vol. 37, pp. 71-98
- [4] Denton, J. D., 1993, "Loss Mechanisms in Turbomachines," The 1993 IGTI Scholar Lecture, *ASME Journal of Turbomachinery*, Vol. 115, pp. 621-656.
- [5] Gier, J., Stubert, B., Brouillet, B. and de Vito, L., 2005, "Interaction of Shrouded Leakage Flow and Main Flow in a Three-Stage LP Turbine," *ASME Journal of Turbomachinery*, Vol. 125, pp. 649-658
- [6] Rosic, B. and Denton, J. D., 2008, "Control of Shroud Leakage Loss by Reducing Circumferential Mixing," *ASME Journal of Turbomachinery*, Vol. 130, pp. 021010-1 – 021010-7
- [7] Wallis, A. M., Denton, J. D. and Demargne A. A. J., 2001, "The Control of Shroud Leakage Flows to Reduce Aerodynamic Losses in a Low Aspect Ratio Shrouded Axial Flow Turbine," *ASME Journal of Turbomachinery*, Vol. 123, pp. 334-341
- [8] Schlienger, J., Kalfas, A. I., Abhari, R. S., 2004, "Vortex-Wake-Blade Interaction in a Shrouded Axial Turbine," *ASME Journal of Turbomachinery*, Vol. 127, pp. 699-707
- [9] Curtis, M. E., Denton, D. J., Longley, P. J. and Budimir, R., 2009, "Controlling Tip Leakage Flow Over a Shrouded Turbine Rotor Using an Air-Curtain," *Proceedings of the ASME*, paper no. GT2009-59411
- [10] Anker, J. E., Mayer J. F. and Casey M. V., 2005, "The Impact of Rotor Labyrinth Seal Leakage Flow on the Loss Generation in an Axial Turbine," *Proceedings of the Institution of Mechanical Engineers, Part A: Journal of Power and Energy*, Vol. 219, pp. 481-490
- [11] Pau, M., Cambuli, F., Mandas, N., 2008, "Shroud Leakage Modeling of the Flow in a Two-Stage Axial Test Turbine," *Proceedings of the ASME*, paper no. GT2008-51093
- [12] Adami, P., Martelli, F., Cecchi, C., 2007, "Analysis of the Shroud Leakage Flow and Mainflow Interactions in High-Pressure Turbines Using an Unsteady Computational Fluid Dynamics Approach," *Proceedings of the Institution of Mechanical Engineers, Part A: Journal of Power and Energy*, Vol. 221, pp. 837-848
- [13] Li, J., Yan, X., LV, Q., Xie, Y. and Feng Z., 2007, "The Effect of the Shrouded Rotor Blade Tip Leakage Flow on the Aerodynamic Performance of a One and Half Turbine Stage," *Challenges of Power Engineering and Environment*, Vol. 5, pp. 275-280.
- [14] Hunter, S. D. and Manwaring, S. R., 2000, "Endwall Cavity Flow Effects on Gas Path Aerodynamics in an Axial Flow Turbine: Part 1 - Experimental and Numerical Investigation," *Proceedings of the ASME*, paper no. 2000-GT-651
- [15] Vakili, A. D., Meganathan, A. J. and Michaud, M., Radhakrishnan, S., 2005, "An Experimental and Numerical Study of Labyrinth Seal Flow," *Proceedings of the ASME*, paper No. GT2005-68224
- [16] Rhode, D. L., Johnson, J. W. and Broussard, D. H., 1997, "Flow Visualization and Leakage Measurements of Stepped Seals: Part 1 – Annular Groove," *ASME Journal of Turbomachinery*, Vol. 119, pp 839-843
- [17] Rhode, D. L., Johnson, J. W. and Broussard, D. H., 1997, "Flow Visualization and Leakage Measurements of Stepped Seals: Part 2 – Sloping Surfaces," *ASME Journal of Turbomachinery*, Vol. 119, pp. 844-848
- [18] Pfau, A., Schlienger, J., Kalfas, A. I. and Abhari, R. S., 2003, "Unsteady Flow Interactions within the Inlet Cavity of a Turbine Rotor Tip Labyrinth Seal," *ASME Journal of Turbomachinery*, Vol. 127, pp. 679-688
- [19] Pfau, A., Kalfas, A. I. and Abhari, R. S., 2004, "Making use of Labyrinth Interaction Flow," *ASME Journal of Turbomachinery*, Vol. 129, pp. 164-174
- [20] Schlienger, J., Pfau, A., Kalfas, A. I. and Abhari, R. S., 2003, "Effects of Labyrinth Seal Variation on Multistage Axial Turbine Flow," *Proceedings of the ASME*, paper no. GT2003-38270
- [21] Tashima, T., Sasaki, T., Kalfas, A. I. and Abhari, R. S., 2007, "Blade Loading Influence on Unsteady Flow Interactions in Axial Steam Turbines," *Proceedings of the ASME*, paper no. GT2007-27452
- [22] Pfau, A., Schlienger, J., Kalfas, A. I. and Abhari, R. S., 2003, "Unsteady, 3-Dimensional Flow Measurement using a Miniature Virtual 4-sensor Fast Response Aerodynamic Probe (FRAP)," *Proceedings of the ASME*, paper no. GT2003-38128
- [23] Lenherr, C., Kalfas, A. I. and Abhari, R. S., 2007, "A Flow Adaptive Aerodynamic Probe Concept For Turbomachinery," *Proceedings of the Institution of Mechanical Engineers, Part A: Journal of Power and Energy*, Vol. 18, pp. 2599-2608
- [24] Barmपालias, K. G., Kalfas, A. I., Abhari, R. S., Hirano, T. and Shibukawa, N., 2010, "Effects of Design Variations of Rotor Entry Cavity Geometry on Shrouded Steam Turbine Performance," *Proceedings of the ASME*, paper no. GT2010-2227